Adjoint-Based Error Estimation and Mesh Adaptation for Stabilized Finite Deformation Elasticity

Brian N. Granzow[b,*], Assad A. Oberai[a], Mark S. Shephard[b]

[a] *Aerospace and Mechanical Engineering*
University of Southern California,
Los Angeles, CA 90089
[b] *Scientific Computation Research Center*
Rensselaer Polytechnic Institute
110 8th Street
Troy, NY 12180

Abstract

Adjoint-based error estimation provides the ability to approximate the discretization error for a functional quantity of interest, such as point-wise displacements or stresses. Mesh adaptation provides the ability to control the discretization error to obtain more accurate solutions while still remaining computationally feasible. In this paper, we develop an approach for adjoint-based error estimation and mesh adaptation for nonlinear finite deformation elasticity using a mixed stabilized finite element method. We apply our developed technique to a well known test case, the Cook's membrane problem, to validate and demonstrate its effectiveness. We then investigate demonstrate the utility of adjoint-based error estimation and mesh adaptation for a three-dimensional example motivated by the study of a cell embedded in a matrix.

Keywords: adjoint, a posteriori, functional, error estimation, adaptation, nonlinear, elasticity, stabilized, finite element

1. Introduction

The purpose of this paper is to develop an approach for functional error estimation and mesh adaptation using adjoint-based techniques for incompressible finite deformation elasticity. An important scenario where incompressible nonlinear elastic materials are utilized is the study of biological soft tissues [23, 29, 10]. Adjoint-based error estimation provides the ability to approximate discretization errors for a functional quantity of interest (QoI) [40, 5, 16, 30, 31, 7, 3], such as point-wise displacements or stresses, or the average displacement over a sub-domain. Mesh adaptation utilizes local information obtained from error estimates to control discretization errors by adaptively modifying the computational mesh.

Previously, in the context of solid mechanics, adaptive adjoint-based error estimation has been used to study linear elasticity in two [34, 38, 17] and three [14] dimensional elasticity, two [35, 36] and three [15] dimensional elasto-plasticity, two dimensional thermoelasticity [32], two dimensional nonlinear elasticity [22], and two dimensional hyperelasticity [43]. In the vast majority of the previous literature, mesh adaptation is performed with structured adaptive mesh refinement using quadrilateral or hexahedral elements. However, for complex geometries such as those that arise in the study of biological tissues, mesh generation and mesh adaptation are reliable, robust, and scalable for simplical elements. This motivates us to consider triangular and tetrahedral elements.

It is well known that solid mechanics problems with incompressibility constraints perform poorly with linear displacement-based Galerkin finite element methods when using simplical elements. This motivates

*Corresponding author, brian.granzow@gmail.com

us to consider a mixed displacement-pressure based finite element formulation with an additional pressure stabilization term. This is in contrast to the work by Whiteley and Tavener [43], who utilized a Taylor-Hood type element to study adjoint-based error estimation in two-dimensional hyperelasticity.

In this work, we propose the following adaptive adjoint-based error estimation strategy. First, we solve the primal finite deformation elasticity problem with a stabilized mixed displacement-pressure finite element method. Next, we construct and solve a discrete adjoint problem in a finer space obtained via uniform mesh refinement. We then estimate the global error in a functional QoI with a scaled discrete adjoint weighted residual error estimate. To localize error estimates to the mesh entity level, we utilize a recently developed approach [37, 44] based on the insertion of partition of unity (PU) into the variational form of the adjoint-weighted residual error representation. Finally, utilizing these localized errors, we perform fully unstructured mesh adaptation utilizing a series of splits, swaps, and collapses.

The contributions of this work can be summarized as follows. First, we expand upon the existing literature in solid mechanics to account for stabilized finite element methods in adjoint-based error estimation. Additionally, we propose a simple error correction to the well-known adjoint-weighted residual [13] error estimate to obtain more accurate error estimates when uniform refinement is used to compute the adjoint solution. Next, we extend the PU-based error localization approach of Richter and Wick [37] to the context of stabilized finite element methods. Finally, we demonstrate that our adaptive adjoint-based error estimation approach can be applied to realistic three-dimensional engineering models, with greater geometric complexity than we have seen in the existing literature.

The remainder of this paper proceeds as follows. First, we review the governing equations for a mixed displacement-pressure based formulation of nonlinear finite deformation elasticity. Next, we review the development of a mixed stabilized finite element method with equal order linear interpolants for displacements and pressures over simplical elements. We then review the so-called adjoint-weighted residual approach for functional error estimation using two discretization levels, as defined by a coarse and a fine space. After this review, We motivate our choice for the fine space, as achieved by uniform mesh refinement. We then introduce a modified, more accurate adjoint-weighted residual error estimate based on an *a priori* analysis. Next, we discuss the localization of the error estimate to the mesh entity level by a recently developed PU approach, which we extend to stabilized finite element methods. We then apply adaptive adjoint-based analysis to a well known test case, the Cook's membrane problem to validate and demonstrate the effectiveness of our approach. We then investigate and demonstrate the utility of adjoint-based error estimation and mesh adaptation for a three-dimensional example, motivated by the study of a cell embedded in a matrix. Finally, we conclude by summarizing our results.

2. Model Problem

In this section, we introduce the governing equations for finite deformation elasticity in a total Lagrangian setting with a neo-Hookean constitutive model. We begin by presenting a mixed pressure-displacement formulation for the strong form of the underlying PDE. We then present the corresponding weak form of the PDE and review the derivation of a stabilized finite element formulation. We conclude by discussing the linearization and solution of the nonlinear system of equations resulting from the stabilized finite element formulation.

2.1. Strong form

Let $\mathcal{B} \subset \mathbb{R}^d$ denote the reference configuration of an open bounded domain with smooth boundary Γ, where d denotes the number of spatial dimensions. Let Γ be decomposed such that $\Gamma = \Gamma_g \cup \Gamma_h$, where $\Gamma_g \cap \Gamma_h = \varnothing$. Let $\boldsymbol{X} \in \mathcal{B}$ denote a point in the reference configuration which, after undergoing some deformation, is located at the point $\boldsymbol{x} \in \mathcal{B}_t$ in the deformed configuration at time t. Let $\boldsymbol{u} := \boldsymbol{x} - \boldsymbol{X}$ denote the displacement vector. The deformation gradient is then defined as $\boldsymbol{F} := \boldsymbol{I} + \frac{\partial \boldsymbol{u}}{\partial \boldsymbol{X}}$, and we denote the determinant of the deformation gradient as $j := \det(\boldsymbol{F})$.

The balance of linear momentum in the absence of inertial and body forces leads to the following boundary value problem in the reference configuration:

$$\begin{cases} -\nabla \cdot \boldsymbol{P} = \boldsymbol{0}, & \boldsymbol{X} \in \mathcal{B}, \\ \boldsymbol{u} = \boldsymbol{g}, & \boldsymbol{X} \in \Gamma_g, \\ \boldsymbol{P} \cdot \boldsymbol{n} = \boldsymbol{h}, & \boldsymbol{X} \in \Gamma_h. \end{cases} \tag{1}$$

Here, $\boldsymbol{P} := j\boldsymbol{\sigma}\boldsymbol{F}^{-T}$ denotes the first Piola-Kirchhoff stress tensor, $\boldsymbol{g}$ denotes an externally applied displacement, $\boldsymbol{h}$ denotes an externally applied traction, $\boldsymbol{n}$ denotes the unit outward normal to the boundary Γ_h, and $\boldsymbol{\sigma}$ denotes the Cauchy stress tensor.

We consider a neo-Hookean constitutive model, where the stress response is characterized by the relationship:

$$\boldsymbol{\sigma} = \underbrace{\mu j^{-\frac{5}{3}} \mathrm{dev}(\boldsymbol{F}\boldsymbol{F}^T)}_{\boldsymbol{\sigma}'} + \underbrace{\frac{\kappa}{2j}(j^2-1)}_{p}\boldsymbol{I}. \tag{2}$$

Here μ denotes the shear modulus, κ denotes the bulk modulus, $\boldsymbol{I}$ is the second order identity tensor, and $\mathrm{dev}(\cdot) := (\cdot) - \frac{1}{3}\mathrm{trace}(\cdot)\boldsymbol{I}$ denotes the deviatoric component of a second order tensor. The stress is decomposed as $\boldsymbol{\sigma} = \boldsymbol{\sigma}' + p\boldsymbol{I}$ into deviatoric and volumetric components, $\boldsymbol{\sigma}'$ and $p\boldsymbol{I}$, respectively.

With this decomposition of the Cauchy stress tensor, the divergence of the first Piola-Kirchhoff stress tensor can be expressed as

$$\begin{aligned} \nabla \cdot \boldsymbol{P} &= \nabla \cdot (j\boldsymbol{\sigma}\boldsymbol{F}^{-T}) \\ &= \nabla \cdot (j(\boldsymbol{\sigma}' + p\boldsymbol{I})\boldsymbol{F}^{-T}) \\ &= \nabla \cdot (j\boldsymbol{\sigma}'\boldsymbol{F}^{-T}) + \nabla \cdot (jp\boldsymbol{F}^{-T}) \\ &= \nabla \cdot (j\boldsymbol{\sigma}'\boldsymbol{F}^{-T}) + j\boldsymbol{F}^{-T}\nabla p. \end{aligned} \tag{3}$$

Here, we have used the Piola identity $\nabla \cdot (j\boldsymbol{F}^{-T}) = 0$ in the fourth equality. Using the decomposition (3) and introducing the pressure (2) as an unknown variable, the model problem (1) can be written in mixed form as:

$$\begin{cases} -\nabla \cdot (j\boldsymbol{\sigma}'\boldsymbol{F}^{-T}) - j\boldsymbol{F}^{-T}\nabla p = 0, & \boldsymbol{X} \in \mathcal{B}, \\ \dfrac{p}{k} - \dfrac{1}{2j}(j^2-1) = 0, & \boldsymbol{X} \in \mathcal{B}, \\ \boldsymbol{u} = \boldsymbol{g}, & \boldsymbol{X} \in \Gamma_g, \\ \boldsymbol{P} \cdot \boldsymbol{n} = \boldsymbol{h}, & \boldsymbol{X} \in \Gamma_h. \end{cases} \tag{4}$$

2.2. Weak Form

Let $\mathcal{V}_u$, $\mathcal{V}_w$, and $\mathcal{V}_p$ denote the displacement trial space, the displacement test space, and the pressure trial and test space, respectively, defined as

$$\mathcal{V}_u := \{\boldsymbol{u} : \boldsymbol{u} \in \mathcal{H}^1(\mathcal{B})^d \ , \ \boldsymbol{u} = \boldsymbol{g} \text{ on } \Gamma_g\}, \tag{5}$$

$$\mathcal{V}_w := \{\boldsymbol{w} : \boldsymbol{w} \in \mathcal{H}^1(\mathcal{B})^d \ , \ \boldsymbol{w} = \boldsymbol{0} \text{ on } \Gamma_g\}, \tag{6}$$

$$\mathcal{V}_p := \{p : p \in L^2(\mathcal{B}) \ \}. \tag{7}$$

Here, $\mathcal{H}^1$ denotes the Sobolev space of square-integrable functions with square integrable first derivatives and L^2 denotes the space of square-integrable functions. The weak form is obtained by multiplying the pressure equation by an arbitrary weighting function $q \in \mathcal{V}_p$ and integrating over the domain $\mathcal{B}$, and by

multiplying the momentum equation by an arbitrary weighting function $\boldsymbol{w} \in \mathcal{V}_w$ and integrating by parts over the domain $\mathcal{B}$. Letting $\mathcal{S} := \mathcal{V}_u \times \mathcal{V}_p$, $\mathcal{V} := \mathcal{V}_w \times \mathcal{V}_p$, $\boldsymbol{U} := [\boldsymbol{u}, p]$, and $\boldsymbol{W} := [\boldsymbol{w}, q]$, this process results in the weak form: find $\boldsymbol{U} \in \mathcal{S}$ such that

$$\mathcal{R}_g(\boldsymbol{W}; \boldsymbol{U}) = 0 \quad \forall\, \boldsymbol{W} \in \mathcal{V}. \tag{8}$$

Here the Galerkin residual $\mathcal{R}_g : \mathcal{V} \times \mathcal{S} \to \mathbb{R}$ is defined as

$$\begin{aligned} \mathcal{R}_g(\boldsymbol{W}; \boldsymbol{U}) := \int_{\mathcal{B}} (j\boldsymbol{\sigma}' \boldsymbol{F}^{-T}) : \nabla \boldsymbol{w} \, \mathrm{d}V + \int_{\mathcal{B}} (jp\boldsymbol{F}^{-T}) : \nabla \boldsymbol{w} \, \mathrm{d}V + \\ \int_{\mathcal{B}} \left[\frac{p}{\kappa} - \frac{1}{2j}(j^2 - 1) \right] q \, \mathrm{d}V - \int_{\Gamma_h} \boldsymbol{h} \cdot \boldsymbol{w} \, \mathrm{d}A. \end{aligned} \tag{9}$$

2.3. Stabilized Finite Element Formulation

Consider a partitioning of the reference domain $\mathcal{B}$ into n_{el} non-overlapping finite element sub-domains $\mathcal{B}_e$ such that $\mathcal{B} = \cup_{e=1}^{n_{el}} \mathcal{B}_e$ and $\mathcal{B}_i \cap \mathcal{B}_j = \varnothing$ if $i \neq j$. Let $\mathcal{V}_u^H \subset \mathcal{V}_u$, $\mathcal{V}_w^H \subset \mathcal{V}_w$, and $\mathcal{V}_p^H \subset \mathcal{V}_p$ denote finite dimensional function spaces defined as:

$$\mathcal{V}_u^H = \{\boldsymbol{u}^H : \boldsymbol{u}^H \in \mathcal{V}_u \ , \ \boldsymbol{u}^H|_{\boldsymbol{X} \in \mathcal{B}_e} \in \mathbb{P}^1(\mathcal{B}_e)^d\}, \tag{10}$$

$$\mathcal{V}_w^H = \{\boldsymbol{w}^H : \boldsymbol{w}^H \in \mathcal{V}_w \ , \ \boldsymbol{w}^H|_{\boldsymbol{X} \in \mathcal{B}_e} \in \mathbb{P}^1(\mathcal{B}_e)^d\}, \tag{11}$$

$$\mathcal{V}_p^H = \{p^H : p^H \in \mathcal{V}_p \ , \ p^H|_{\boldsymbol{X} \in \mathcal{B}_e} \in \mathbb{P}^1(\mathcal{B}_e)\} \tag{12}$$

Here $\mathbb{P}^1(\mathcal{B}_e)$ denotes the space of piecewise linear polynomials over elements $\mathcal{B}_e$, $e = 1, 2, \ldots, n_{el}$.

We follow the approach of Maniatty et al. [21, 26, 33] to obtain a stabilized Petrov-Galerkin finite element formulation of the primal problem. This approach proceeds by multiplying the momentum equation by a perturbed weighting function of the form $\boldsymbol{w}^H + \tau_e \boldsymbol{F}^{-T} \nabla q^H$ and integrating over the reference domain $\mathcal{B}$, and by multiplying the pressure equation by a weighting function q^H and integrating over the domain $\mathcal{B}$.

Here $\tau_e = \frac{c_0 H_e^2}{2\mu}$ is a mesh-dependent stabilization parameter, where $H_e = \mathrm{meas}(\mathcal{B}_e)$ denotes a characteristic size of a given mesh element, μ denotes the shear modulus, c_0 denotes a non-dimensional, non-negative stability constant, $\boldsymbol{w}^H \in \mathcal{V}_w^H$ is a displacement weighting function, and $q^H \in \mathcal{V}_p^H$ is a pressure weighting function. Additionally, $\boldsymbol{F}^{-T} \nabla q^H$ represents the pull-back of the gradient of the pressure weighting function to the reference configuration.

This yields the following problem: find $(\boldsymbol{u}^H, p^H) \in (\mathcal{V}_u^H, \mathcal{V}_p^H)$ such that for all $(\boldsymbol{w}^H, q^H) \in (\mathcal{V}_w^H, \mathcal{V}_p^H)$

$$\begin{aligned} -\int_{\mathcal{B}} (\nabla \cdot \boldsymbol{P}) \cdot \boldsymbol{w}^H \, \mathrm{d}V + \int_{\mathcal{B}} \left[\frac{p^H}{\kappa} - \frac{1}{2j}(j^2 - 1) \right] q^H \, \mathrm{d}V - \\ \sum_{e=1}^{n_{el}} \int_{\mathcal{B}_e} (\nabla \cdot \boldsymbol{P}) \cdot (\tau_e \boldsymbol{F}^{-T} \nabla q^H) \, \mathrm{d}V = 0. \end{aligned} \tag{13}$$

The first two terms on the left hand side of equation (13) yield the Galerkin residual $\mathcal{R}_g(\boldsymbol{W}^H; \boldsymbol{U}^H)$ after integrating the left-most term by parts. The integrand of the third term on left hand side of equation (13) can be expressed as

$$\begin{aligned} (\nabla \cdot \boldsymbol{P}) \cdot (\tau_e \boldsymbol{F}^{-T} \nabla q^H) \ = (\nabla \cdot j\boldsymbol{\sigma}' \boldsymbol{F}^{-T}) \cdot (\tau_e \boldsymbol{F}^{-T} \nabla q^H) + \\ (\tau_e j \boldsymbol{F}^{-1} \boldsymbol{F}^{-T}) : (\nabla p^H \otimes \nabla q^H). \end{aligned} \tag{14}$$

We remark that the first term in the right hand side of equation (14) evaluates to zero for simplical elements with linear shape functions, which we presently consider.

Let $\mathcal{S}^H = \mathcal{V}_u^H \times \mathcal{V}_p^H$, $\mathcal{V}^H = \mathcal{V}_w^H \times \mathcal{V}_p^H$, $\boldsymbol{U}^H = [\boldsymbol{u}^H, p^H]$, and $\boldsymbol{W}^H = [\boldsymbol{w}^H, q^H]$. Using equations (9) and (14) in the perturbed weak problem (13), we arrive at the stabilized finite element formulation: find $\boldsymbol{U}^H \in \mathcal{S}^H$ such that

$$\mathcal{R}_g(\boldsymbol{W}^H; \boldsymbol{U}^H) + \mathcal{R}_\tau(\boldsymbol{W}^H; \boldsymbol{U}^H) = 0 \quad \forall\, \boldsymbol{W}^H \in \mathcal{V}^H. \tag{15}$$

Here $\mathcal{R}_\tau : \mathcal{V}^H \times \mathcal{S}^H \to \mathbb{R}$ is the residual corresponding to the additional pressure stabilization, given by:

$$\mathcal{R}_\tau(\boldsymbol{W}^H; \boldsymbol{U}^H) := \sum_{e=1}^{n_{el}} \int_{\mathcal{B}_e} \tau_e (j \boldsymbol{F}^{-1} \boldsymbol{F}^{-T}) : (\nabla p^H \otimes \nabla q^H)\, \mathrm{d}V. \tag{16}$$

We remark that we have introduced a consistent stabilization term, in that $\mathcal{R}_\tau \to 0$ as $H \to 0$.

2.4. Linearization and Solution Strategy

The stabilized finite element formulation (15) posed in residual form leads to a system of N nonlinear algebraic equations $\boldsymbol{R}^H : \mathbb{R}^N \to \mathbb{R}^N$, such that the numerical solution vector $\boldsymbol{U}^H \in \mathbb{R}^N$ of nodal coefficients satisfies

$$\boldsymbol{R}^H(\boldsymbol{U}^H) = \boldsymbol{0}. \tag{17}$$

We compute consistent element-level tangent stiffness matrices via automatic differentiation [8] of element-level contributions to the residual vector $\boldsymbol{R}^H$ to assemble the system Jacobian $\boldsymbol{\mathcal{J}}^H \in \mathbb{R}^{N \times N}$, defined as

$$\boldsymbol{\mathcal{J}}^H(\boldsymbol{U}^H) := \left. \frac{\partial \boldsymbol{R}^H}{\partial \boldsymbol{U}^H} \right|_{\boldsymbol{U}^H}. \tag{18}$$

The full nonlinear problem (17) is then solved with Newton's method, where we iterate over the steps

$$\begin{aligned} \boldsymbol{\mathcal{J}}^H(\boldsymbol{U}_k^H)\, \delta \boldsymbol{U}_k^H &= -\boldsymbol{R}^H(\boldsymbol{U}_k^H) \\ \boldsymbol{U}_{k+1}^H &= \boldsymbol{U}_k^H + \delta \boldsymbol{U}_k^H, \end{aligned} \tag{19}$$

until the convergence criterion $\|\boldsymbol{R}^H(\boldsymbol{U}^H)\|_2 < \epsilon$ is satisfied for some user-specified tolerance ϵ. Here $\boldsymbol{U}_k^H$ denotes the solution vector at the k^{th} Newton iteration and $\delta \boldsymbol{U}_K^H$ denotes the incremental update at the k^{th} iteration obtained by solving the Newton linear system.

3. Adjoint-Based Error Estimation

In this section we derive an adjoint-based error estimation strategy to compute errors in functional quantities of interest. We begin by reviewing functional error estimation with two discretization levels, defined by a *coarse* space and a *fine* space. Next, we discuss and motivate our choice for the fine space. We then introduce a modified, more accurate functional error estimate based on a simple *a priori* analysis. Finally, we conclude by discussing how we localize the functional error to *correction indicators* at the mesh entity level.

3.1. Two-Level Error Estimation

Let $J(\boldsymbol{U})$ denote a functional quantity that is of physical significance. We adopt a two-level error estimation strategy [40, 41, 42, 13] to estimate the discretization error in J. This strategy proceeds by defining a *coarse* space, defined in the present setting by the spaces $(\mathcal{S}^H, \mathcal{V}^H)$, and a *fine* space, $(\mathcal{S}^h, \mathcal{V}^h)$.

In addition to the system of nonlinear algebraic equations (17) defined on the coarse space $(\mathcal{S}^H, \mathcal{V}^H)$, the stabilized finite element formulation (15) posed in residual form on the fine space $(\mathcal{S}^h, \mathcal{V}^h)$ leads to a system of n nonlinear algebraic equations $\boldsymbol{R}^n : \mathbb{R}^n \to \mathbb{R}^n$ on the fine space, such that

$$\boldsymbol{R}^h(\boldsymbol{U}^h) = \boldsymbol{0}, \tag{20}$$

where $\boldsymbol{U}^h \in \mathbb{R}^n$ is understood to be the solution vector of nodal coefficients for the fine problem (20). Here $n > N$. Similarly, the functional quantity of interest can be discretized on the coarse and fine spaces, resulting in $J^H : \mathbb{R}^N \to \mathbb{R}$ and $J^h : \mathbb{R}^n \to \mathbb{R}$, respectively.

Let $\boldsymbol{U}_H^h = \boldsymbol{I}_H^h \boldsymbol{U}^H$ denote the prolongation of the coarse solution $\boldsymbol{U}^H$ onto the fine space $\mathcal{S}^h$ via interpolation, where $\boldsymbol{I}_H^h : \mathcal{S}^H \to \mathcal{S}^h$. The residual equations on the coarse space can be expanded in a Taylor series about the prolongated coarse solution as

$$\boldsymbol{R}^h(\boldsymbol{U}^h) = \boldsymbol{R}^h(\boldsymbol{U}_H^h) + \left[\frac{\partial \boldsymbol{R}^h}{\partial \boldsymbol{U}^h}\bigg|_{\boldsymbol{U}_H^h}\right](\boldsymbol{U}^h - \boldsymbol{U}_H^h) + \dots \tag{21}$$

and similarly, the functional evaluated on the coarse space can be expanded about the prolongated coarse solution as

$$J^h(\boldsymbol{U}^h) = J^h(\boldsymbol{U}_H^h) + \left[\frac{\partial J^h}{\partial \boldsymbol{U}^h}\bigg|_{\boldsymbol{U}_H^h}\right](\boldsymbol{U}^h - \boldsymbol{U}_H^h) + \dots \tag{22}$$

Using equation (20), the discretization error between the two spaces can be approximated to first order as

$$(\boldsymbol{U}^h - \boldsymbol{U}_H^h) \approx -\left[\frac{\partial \boldsymbol{R}^h}{\partial \boldsymbol{U}^h}\bigg|_{\boldsymbol{U}_H^h}\right]^{-1} \boldsymbol{R}^h(\boldsymbol{U}_H^h). \tag{23}$$

This approximation can then be substituted into the functional Taylor expansion (22) to yield the so-called adjoint weighted residual,

$$J^h(\boldsymbol{U}^h) - J^h(\boldsymbol{U}_H^h) \approx -\underbrace{\left[\frac{\partial J^h}{\partial \boldsymbol{U}^h}\bigg|_{\boldsymbol{U}_H^h}\right]\left[\frac{\partial \boldsymbol{R}^h}{\partial \boldsymbol{U}^h}\bigg|_{\boldsymbol{U}_H^h}\right]^{-1}}_{\boldsymbol{Z}^h} \boldsymbol{R}^h(\boldsymbol{U}_H^h), \tag{24}$$

where $\boldsymbol{Z}^h \in \mathbb{R}^n$ denotes the solution to the *adjoint problem*:

$$\left[\frac{\partial \boldsymbol{R}^h}{\partial \boldsymbol{U}^h}\bigg|_{\boldsymbol{U}_H^h}\right]^T \boldsymbol{Z}^h = \left[\frac{\partial J^h}{\partial \boldsymbol{U}^h}\bigg|_{\boldsymbol{U}_H^h}\right]^T. \tag{25}$$

3.2. Choice of Fine Space

Several options exist for the choice of the fine space and the approximation of the adjoint problem (25). The fine space can be defined by uniformly refining the mesh, which we will refer to as h-enrichment, increasing the polynomial interpolation order, which we will refer to as p-enrichment, uniformly refining the mesh and increasing the polynomial order, which we will refer to as hp-enrichment, or by considering a finer space provided by variational multiscale techniques [18].

It is common to solve the adjoint problem (25) in the coarse space and then perform a reconstruction process to recover an approximation of the adjoint solution on the fine space [27, 25, 12, 5]. However, the most commonly used choices for reconstruction do not incorporate the underlying physics of the problem, and thus are not guaranteed to result in a more accurate approximation of the adjoint solution [13]. This motivates us to solve the adjoint problem globally on the fine space [4, 19].

In the present work, we choose h-enrichment for the fine space. Along with the previously discussed accuracy considerations, we are motivated to do so for two additional reasons. First, the use of a higher order basis ala p-enrichment would necessitate the inclusion of the neglected higher order stabilization term in the expansion (14). This term is generally non-trivial to implement [26]. Second, we remark that higher-order stabilized finite element methods with equal order interpolants are rarely used in practice, as one could use a Taylor-Hood type element [39] to satisfy the Babuška-Brezzi condition with much fewer degrees of freedom than the corresponding stabilized finite element method with equal order interpolants.

3.3. Modified Functional Error Estimate

Consider that the functional of interest converges at the rate k, such that $J(\boldsymbol{U}) - J^h(\boldsymbol{U}_H^h) = cH^k$ and $J(\boldsymbol{U}) - J^h(\boldsymbol{U}^h) = ch^k$, where $J(\boldsymbol{U})$ is the exact value of the functional quantity of interest. We assume that the fine space is obtained via mesh refinement, such that $\frac{h}{H} = \frac{1}{2}$. Consider the ratio

$$\begin{aligned}\frac{J^h(\boldsymbol{U}^h) - J^h(\boldsymbol{U}_H^h)}{J(\boldsymbol{U}) - J^h(\boldsymbol{U}_H^h)} &= \frac{\left[J(\boldsymbol{U}) - J^h(\boldsymbol{U}_H^h)\right] - \left[J(\boldsymbol{U}) - J^h(\boldsymbol{U}^h)\right]}{J(\boldsymbol{U}) - J^h(\boldsymbol{U}_H^h)} \\ &= \frac{cH^k - ch^k}{cH^k} \\ &= 1 - \left(\frac{h}{H}\right)^k \\ &= 1 - \left(\frac{1}{2}\right)^k\end{aligned} \tag{26}$$

in the limit as $H \to 0$ [13]. We denote this ratio as $\alpha := 1 - (1/2)^k$. Let η denote an approximation to the functional error $J(\boldsymbol{U}) - J^h(\boldsymbol{U}_H^h)$. Let $\mathcal{I}$ denote the effectivity index given by

$$\mathcal{I} = \frac{\eta}{J(\boldsymbol{U}) - J^h(\boldsymbol{U}_H^h)}. \tag{27}$$

Naturally, we would like to obtain error estimates η that lead to effectivity indices of $\mathcal{I} = 1$ as $H \to 0$. To this end, we recall that $J^h(\boldsymbol{U}^h) - J^h(\boldsymbol{U}_H^h) \approx -\boldsymbol{Z}^h \cdot \boldsymbol{R}^h(\boldsymbol{U}_H^h)$ from equation (24) and obtain the scaled adjoint weighted residual error estimate

$$\eta = -\frac{1}{\alpha}\boldsymbol{Z}^h \cdot \boldsymbol{R}^h(\boldsymbol{U}_H^h). \tag{28}$$

3.4. Error Localization

To drive mesh adaptation, it is necessary to localize contributions to the total error η to the mesh entity level to obtain *correction indicators*. One commonly used approached for finite volume and discontinuous Galerkin methods proceeds by considering a decomposition of the error estimate (28) into a sum of discrete adjoint weighted residuals over elements in the fine mesh. However, this approach is not optimal for continuous finite elements as it does not account for systematic inter-element cancellation, and the sum of the resulting correction indicators would lead to a considerable over-estimation of the functional error [13]. This, in turn, would lead to a sub-optimal adaptive strategy.

Traditional adjoint-weighted residual error estimates for continuous Galerkin finite element methods proceed by integrating the left hand side of equation (15) by parts over individual elements to recover strong-form volumetric and jump term contributions to the error. In this work, we utilize a recently introduced localization strategy by Richter and Wick [37] for its straightforward implementation and because it allows us to automate the adaptive process. In this localization, adjoint-weighted residual error information from neighboring elements is gathered by introducing a partition of unity, leading to nodally-based correction indicators. In the context of solid mechanics, this approach has been used successfully for phase field fracture [44]. In this section, we extend this variational localization technique to stabilized finite element methods.

We begin by reviewing adjoint-based error estimation for stabilized finite element methods in a continuous setting, as outlined by Cyr et al. [9], for which we introduce the continuous linearized adjoint problem: find $\boldsymbol{Z} \in \mathcal{V}$ such that

$$\mathcal{R}'_g[\boldsymbol{U}^H](\boldsymbol{V}, \boldsymbol{Z}) = J'[\boldsymbol{U}^H](\boldsymbol{V}) \quad \forall\, \boldsymbol{V} \in \mathcal{V}. \tag{29}$$

Here, the prime indicates Fréchet linearization with respect to the argument in the square brackets. The adjoint solution $\boldsymbol{Z} := [\boldsymbol{z}_u, z_p]$ is defined as a vector of the adjoint variable $\boldsymbol{z}_u$ corresponding to the primal

displacement $\boldsymbol{u}$ and the adjoint variable z_p corresponding to the primal pressure p. The variable $\boldsymbol{U}^H$ denotes the solution to the stabilized finite element problem (15) on the coarse space.

Let $\boldsymbol{E} := \boldsymbol{U} - \boldsymbol{U}^H$ denote the discretization error. With the introduction of the adjoint problem (29), a functional error representation can be derived in the following manner:

$$\begin{aligned} J(\boldsymbol{U}) - J(\boldsymbol{U}^H) &= J'[\boldsymbol{U}^H](\boldsymbol{E}) + \mathcal{O}(\boldsymbol{E}^2) \\ &= \mathcal{R}'_g[\boldsymbol{U}^H](\boldsymbol{E}, \boldsymbol{Z}) + \mathcal{O}(\boldsymbol{E}^2) \\ &= \mathcal{R}_g(\boldsymbol{Z}; \boldsymbol{U}) - \mathcal{R}_g(\boldsymbol{Z}; \boldsymbol{U}^H) + \mathcal{O}(\boldsymbol{E}^2) \\ &= -\mathcal{R}_g(\boldsymbol{Z}; \boldsymbol{U}^H) + \mathcal{O}(\boldsymbol{E}^2) \\ &= -\mathcal{R}_g(\boldsymbol{Z} - \boldsymbol{Z}^H; \boldsymbol{U}^H) + \mathcal{R}_\tau(\boldsymbol{Z}^H; \boldsymbol{U}^H) + \mathcal{O}(\boldsymbol{E}^2). \end{aligned} \tag{30}$$

Here the first equality is due to the linearization [5] of the functional J, the second equality is due to the definition of the adjoint problem (29), the third equality is due to the linearization [5] of the Galerkin residual semilinear form R_g, the fourth equality is due to Galerkin orthogonality, and the fifth equality holds by the definition of the stabilized finite element method (15). The variable $\boldsymbol{Z}^H$ denotes the interpolant of the adjoint solution $\boldsymbol{Z}$ onto the coarse finite element space $\mathcal{S}^H$.

Let $\boldsymbol{Z}^h$ denote the solution to the discrete adjoint problem (25) solved on the fine space. We assume that this solution well approximates the continuous adjoint problem (29), such that $\boldsymbol{Z} \approx \boldsymbol{Z}^h$. The functional error is then approximated by neglecting higher order terms to obtain

$$J(\boldsymbol{U}) - J(\boldsymbol{U}^H) \approx -\mathcal{R}_g(\boldsymbol{Z}^h - \boldsymbol{Z}^H; \boldsymbol{U}^H) + \mathcal{R}_\tau(\boldsymbol{Z}^H, \boldsymbol{U}^H). \tag{31}$$

Following the approach of Richter and Wick [37], we introduce a partition of unity $\sum_i \phi_i = 1$ into the weighting function slot for the error estimate to localize the error. In this work, this partition of unity is realized with linear Lagrange basis functions. This yields local level error contributions η_i at the n_{vtx} mesh vertices in the fine mesh, given as

$$J(\boldsymbol{U}) - J(\boldsymbol{U}^H) \approx \sum_{i=1}^{n_{vtx}} \underbrace{-\mathcal{R}_g((\boldsymbol{Z}^h - \boldsymbol{Z}^H)\phi_i \,;\, \boldsymbol{U}^H) + \mathcal{R}_\tau(\boldsymbol{Z}^H\phi_i \,;\, \boldsymbol{U}^H)}_{\eta_i}. \tag{32}$$

We compute an approximate upper bound on the error by summing the absolute value of the error contributions over all mesh vertices.

$$\hat{\eta} = \sum_{i=1}^{n_{vtx}} |\eta_i|. \tag{33}$$

To compute an element-based correction indicator η_e, we interpolate the value of the vertex-based error contributions η_i to element centers and then take the result's absolute value.

4. Mesh Adaptation

To control discretization errors, we make use of conforming unstructured mesh adaptation. Mesh adaptation provides the means to modify the spatial discretization of the domain $\mathcal{B}$ such that the degrees of freedom are nearly optimally distributed with respect to the calculation of the QoI. We utilize the PUMI [20] software suite to perform a series of edge splits, swaps, and collapses [24, 1] to satisfy the input of a *mesh size field*. For isotropic mesh adaptation, which we presently consider, the mesh size field is defined as a scalar field that defines element edge lengths over the mesh. From a high-level, we would like to specify a mesh size field that refines in areas of the domain that strongly contribute to the error and coarsens the mesh in areas that are insensitive to the error.

To this end, we utilize a size field specification following Boussetta et al. [6] that attempts to equidistribute the error in an output adapted mesh with N target elements. Let p be the polynomial interpolant

order for the chosen finite element method. In the present setting, $p = 1$. We first define the global quantity G as

$$G = \sum_{e=1}^{n_{el}} (\eta_e)^{\frac{2d}{2p+d}}. \tag{34}$$

Using this computed quantity, new element mesh sizes H_e^{new} are determined by scaling the previous element size H_e according to the formula

$$H_e^{\text{new}} = \left(\frac{G}{N}\right)^{\frac{1}{d}} (\eta_e)^{\frac{-2}{2p+d}} H_e \tag{35}$$

Additionally, to prevent excessive refinement or coarsening in a single adaptive step, we clamp the element size such that it is no smaller than one quarter and no greater than twice the previous element size,

$$\frac{1}{4} \leq \frac{H_e^{\text{new}}}{H_e} \leq 2. \tag{36}$$

As a further explanation, this clamping is performed to ensure that mesh adaptation is being driven by accurate correction indicators. That is, if the mesh were too heavily modified during a single adaptive iteration, the localized correction indicators would begin to lose accuracy on the modified mesh.

5. Results

5.1. Cook's Membrane

In this section, we investigate two displacement-based quantities of interest for Cook's membrane. The first QoI we consider is the y-component of displacement at the point $\boldsymbol{X}_0 = (44, 55)$ such that $J_1(\boldsymbol{U}) = \int_{\mathcal{B}} \delta(\boldsymbol{X} - \boldsymbol{X}_0)\ u_y \,\mathrm{d}V$. The second QoI we consider is the average displacement over the entire domain, such that $J_2(\boldsymbol{U}) = \int_{\mathcal{B}} \frac{1}{2}(u_x + u_y) \,\mathrm{d}V$. Figure 1 shows the geometry and loading conditions for the Cook's membrane problem, where the left-most boundary is fixed in the x and y directions and a purely vertical traction of magnitude 10 is applied to the right-most boundary. For material properties, we choose the elastic modulus to be $E = 1000$ and Poisson's ratio as $\nu = 0.4999$, such that the material nearly incompressible. We choose the stabilization parameter to be $c_0 = 1$. For both quantities of interest, we expect the convergence rate to be $k = 2$, such that the scaling parameter $\alpha = \frac{3}{4}$.

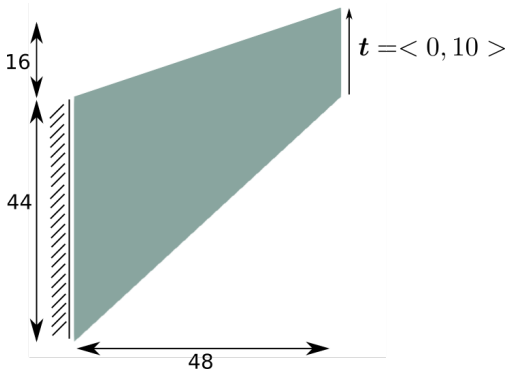

Figure 1: Cook's membrane problem definition.

For each QoI, an initial mesh with a uniform size of $H = 8$ was generated. Figures 3 and 4 show the initial mesh utilized for both the point-wise and average displacement QoIs. From these initial meshes, the steps

Solve primal PDE → Solve adjoint PDE → Localize error → Adapt mesh

were iteratively performed until a final mesh with about $10,000$ degrees of freedom was produced. During each mesh adaptation, the size field was specified according to the equation (35) such that the desired number of elements N in the output mesh is twice the number of elements in the previous mesh.

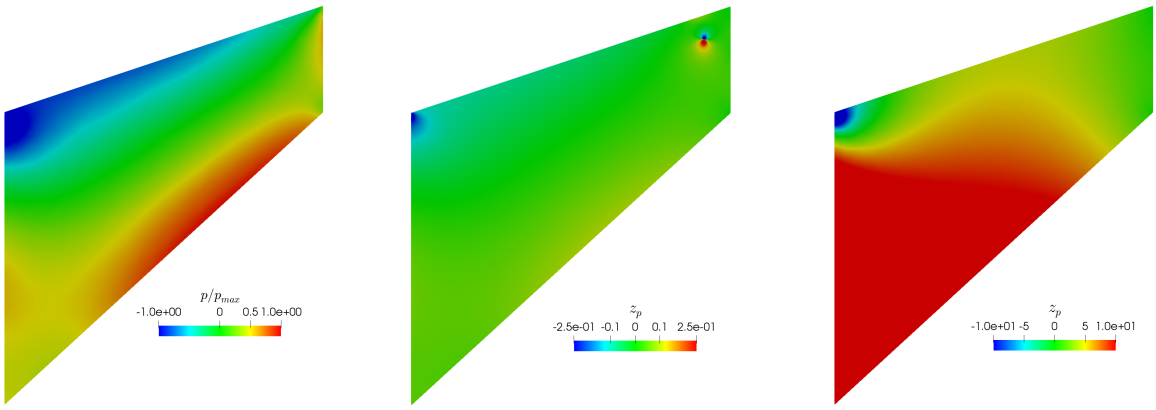

Figure 2: The pressure component p of the primal solution scaled by its maximal value (left), the pressure component z_p of the adjoint solution for the point-wise QoI $J_1(\boldsymbol{U})$, and the pressure component z_p of the adjoint solution for the average displacement QoI $J_2(\boldsymbol{U})$.

The left-most figure of Figure 2 illustrates the pressure component p of the primal solution scaled by its maximal value. We remark that this result is consistent with previous literature [28]. The center and right-most figures of Figure 2 shows the pressure component z_p of the adjoint solution for the point-wise QoI $J_1(\boldsymbol{U})$ and the average displacement QoI $J_2(\boldsymbol{U})$, respectively. For the point-wise QoI, the adjoint solution z_p is highly localized to the point that defines the QoI and the corner of stress singularity.

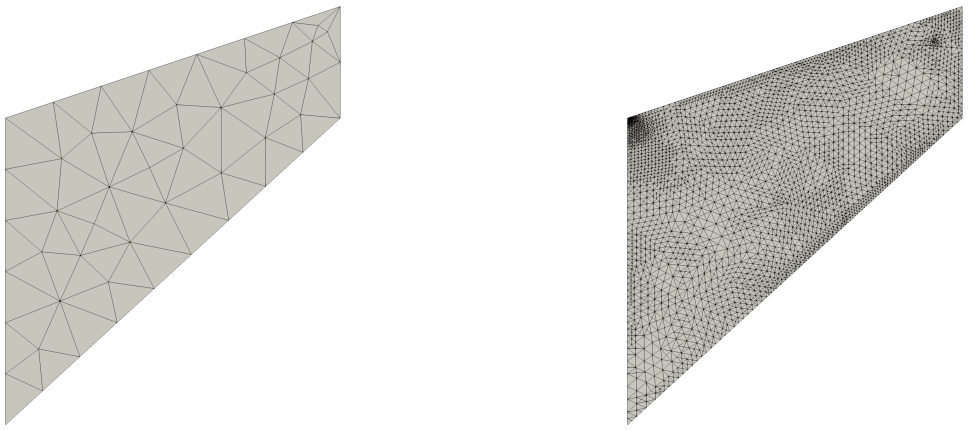

Figure 3: Initial mesh (left) and adapted mesh (right) at the fifth adaptive iteration for the Cook's membrane problem with the point-wise QoI $J_1(\boldsymbol{U})$.

To approximate the exact values of the quantities of interest, the primal problem was solved on a "truth" mesh with about 1.5 million degrees of freedom. This mesh is finer at every spatial location than the final meshes produced by the two adaptive simulations. The reference value for the point-wise QoI on the truth mesh was computed to be $J_1(\boldsymbol{U}) = 2.395627$ and the reference value for the average displacement QoI was computed to be $J_2(\boldsymbol{U}) = 324.0948$.

We consider two different errors, the "exact error" $\mathcal{E} = J(\boldsymbol{U}) - J^h(\boldsymbol{U}_H^h)$ and the error $\mathcal{E}_h = J^h(\boldsymbol{U}^h) - J^h(\boldsymbol{U}_H^h)$ with respect to the functional evaluated on the fine mesh with mesh size $\frac{H}{2}$. Here we place quotations

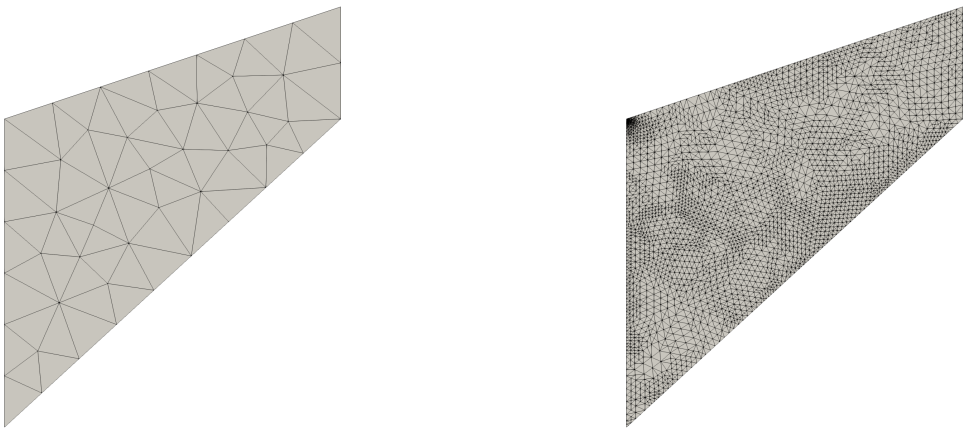

Figure 4: Initial mesh (left) and adapted mesh (right) at the fifth adaptive iteration for the Cook's membrane problem with the average displacement QoI $J_2(\boldsymbol{U})$.

around the term "exact error" because we have only approximated $J(\boldsymbol{U})$ with high fidelity and have not obtained its actual exact value. We recall the effectivity index (27) defined as $\mathcal{I} = \frac{\eta}{\mathcal{E}}$ and additionally define a discrete effectivity index as $I_h = \frac{\eta}{\mathcal{E}_h}$. An effecitivty index of $\mathcal{I} = 1$ indicates that the error estimate η has exactly recovered the "true error". Similarly, a discrete effectivity index of $\mathcal{I}_h = 1$ indicates that the error estimate η has exactly recovered the error between the functional evaluated on the fine space and the functional evaluated on the coarse space. Figure 5 plots the effectivity $\mathcal{I}$ relative to the "exact error" and the effectivity $\mathcal{I}_h$ relative to the fine-space error, and demonstrates the ability of η to effectively estimate the error as $H \to 0$ during the adaptive process for the chosen functional quantities. The small distance away from 1 in the discrete effectivity index $\mathcal{I}_h$ represents the linearization error associated with the estimate η, introduced by the linearized adjoint problem (25).

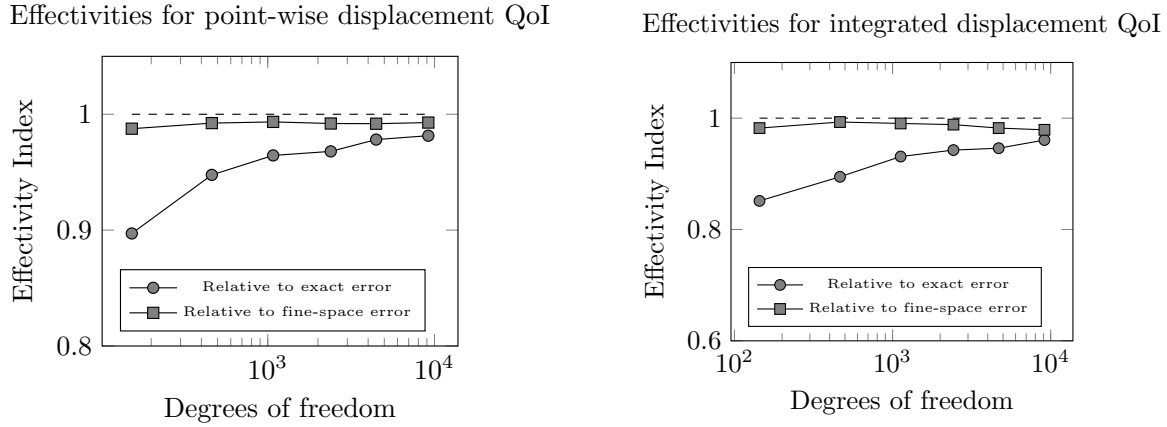

Figure 5: Effectivities for the point-wise QoI $J_1(\boldsymbol{U})$ (left) and for the average displacement QoI $J_2(\boldsymbol{U})$ (right) for the Cook's membrane problem.

Figure 6 demonstrates the evolution of various errors throughout the adaptive process. First, we note that the "exact error" $\mathcal{E}$ and the estimated error η are very close, as previously discussed. Next, we note that the estimated bound $\hat{\eta}$ on the functional error, computed as the sum of localized error contributions, overestimates the error, but only by a small factor. This provides some justification to expect that the

derived correction indicators are well-suited to drive mesh adaptation. Finally, we remark that an improved corrected functional value $J^*(\boldsymbol{U}_H^h)$ can be computed as the approximated functional value plus the estimated error, $J^*(\boldsymbol{U}_H^h) = J^h(\boldsymbol{U}_H^h) + \eta$. This corrected value tends to converge at a faster rate than the computed value $J^h(\boldsymbol{U}_H^h)$. In particular, this corrected value can prove valuable for coarser discretizations, where the error in the corrected value is around two orders of magnitude smaller than the error in the computed value of the functional.

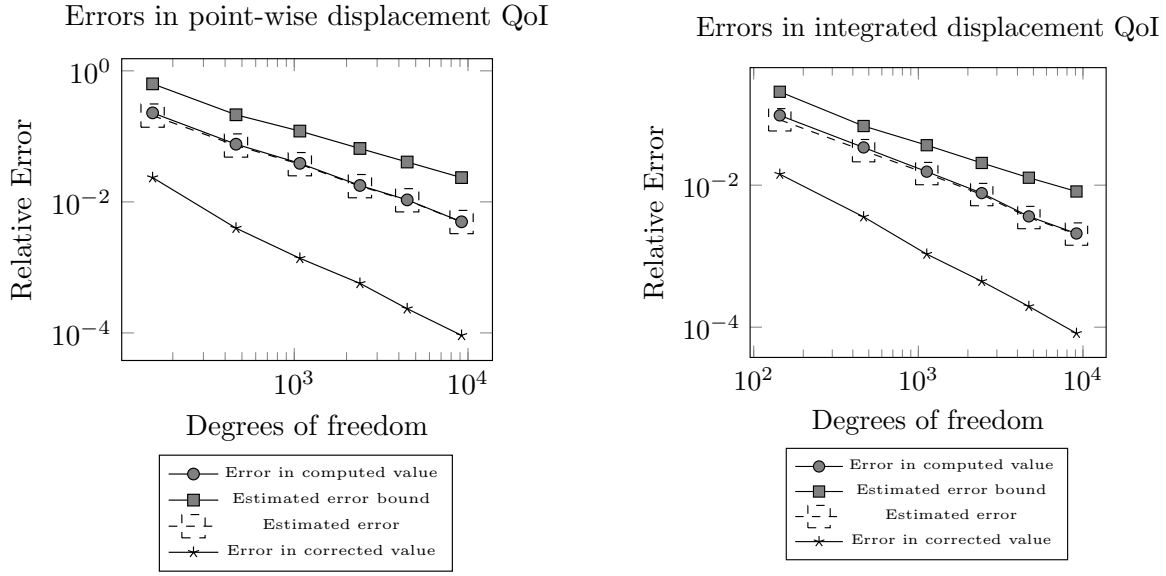

Figure 6: Errors for the point-wise QoI $J_1(\boldsymbol{U})$ (left) and for the average displacement QoI $J_2(\boldsymbol{U})$ (right) for the Cook' membrane problem.

Figure 3 shows the adapted mesh after 5 adaptive cycles for the point-wise QoI. We first note that the mesh is heavily refined in the upper left corner of the mesh, where there is a stress singularity. Without accurately resolving this singularity, so-called "pollution error" [2] will affect the accuracy of the finite element solution throughout the domain. This demonstrates that the adaptive adjoint-based procedure accurately identifies other sources of error that must be resolved even when a fully localized QoI is chosen. Similarly, Figure 4 shows the adapted mesh after 5 adaptive cycles for the average displacement QoI. Again there is heavy refinement in the corner with the stress singularity.

Interestingly, Figure 3 also illustrates that the adjoint-based adaptive procedure refines around the spatial location that defines the point-wise QoI. This may, in part, be explained by the fact that the data driving the adjoint problem is a discrete delta function. However, such refinement is unlikely to lead to an optimal distribution of degrees of freedom in the mesh. In essence, the Cook's membrane problem is a cantilever beam and this result indicates that we must refine heavily at the end of the beam in order to accurately evaluate displacements at the beam tip. This is antithetical to engineering intuition and experience. Another factor leading to this result may be our choice of error localization. We have localized the error based on a PU-based weak form statement (32), where derivatives are left on the weighting function term $\boldsymbol{Z}$. This, in turn, may lead to a heavier emphasis on the local point-wise location during the adaptive process. We leave investigation into this area as an avenue for future study.

5.2. A Cell Embedded in a Matrix

In this section, we apply adjoint-based error estimation and mesh adaptation to a three-dimensional problem that arises in the study of cellular biomechanics and mechanobiology. The problem of interest

involves investigating a cell embedded in an extracellular matrix. The traction that this cell exerts on its surroundings directly influences cellular processes like migration and differentiation. Recently, Dong and Oberai [11] introduced a process to recover cellular tractions based on the solution of an *inverse* problem. For this inverse problem, it is assumed that displacements throughout the extracellular matrix are given with some uncertainty, and successive solutions of a *forward* problem are solved to recover the tractions driving the problem. Presently, we focus on accurately solving the forward problem in this process using adjoint-based error estimation. That is, given tractions imposed on the cellular membrane, we would like to solve for displacements in some region of the domain as accurately as possible.

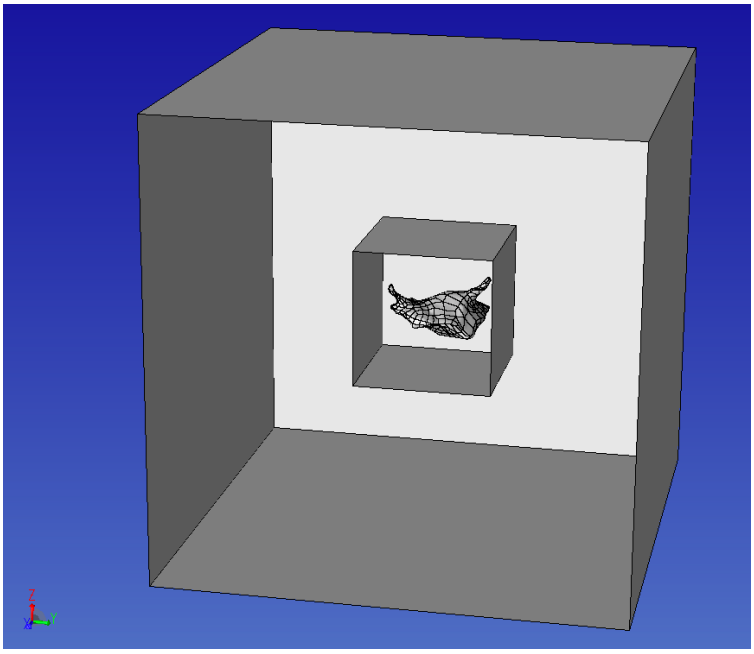

Figure 7: The computational geometry for the microglial cell problem. The inner-most surface represents the geometry of the microgial cell, the outer-most bounding box represents the extracellular matrix in which the cell is embedded, and the inner bounding box represents the domain over which the local average displacement QoI $J(\boldsymbol{U})$ is defined.

Specifically, we focus on a microglial cell with dimensions of about $20\mu m \times 20\mu m \times 20\mu m$ embedded in an extracellular matrix of dimension $100\mu m \times 100\mu m \times 100\mu m$. We choose the QoI to be a local average displacement, $J(\boldsymbol{U}) = \int_{\mathcal{B}_0} \frac{1}{3}(u_x + u_y + u_z)\,\mathrm{d}V$, defined over a $30\mu m \times 30\mu m \times 30\mu m$ bounding box $\mathcal{B}_0$ surrounding the microglial cell. Figure 7 shows the geometry defining the microglial cell, the extracellular matrix, and the local QoI domain $\mathcal{B}_0$. For the extracellular matrix, the shear modulus $\mu = \frac{E}{2(1+\nu)}$ is set to be 600 Pa and Poisson's ratio is set to be $\nu = 0.4999$, which is consistent with material properties for hydrogels [23, 29, 10].

To drive the problem, we impose traction boundary conditions along the surface of the microglial cell. The magnitude of the traction $\boldsymbol{h}$ is defined to be 10 times the distance to the center of the microglial cell and its direction points inward toward the center of the microglial cell. The applied traction is shown in Figure 8. This traction serves to pull the extracellular matrix inwards towards the center of the microglial cell, which is consistent with observed physical behavior [11]. The deformation of the cell surface due to this applied traction is shown in Figure 9. To constrain rigid body translations and rotations, we prescribe displacements $u_x = 0$ on the face with constant minimum x-coordinate value, $u_y = 0$ on the face with constant minimum y-coordinate value, and $u_z = 0$ on the face with constant minimum z-coordinate value. As a reference value for the average displacement QoI, the primal problem was solved on a "truth" mesh with about 60 million degrees of freedom. The reference value for the QoI was computed to be $J(\boldsymbol{U}) = -527.1453$.

An initial mesh with about $30,000$ degrees of freedom was generated, as shown in Figure 10. From this

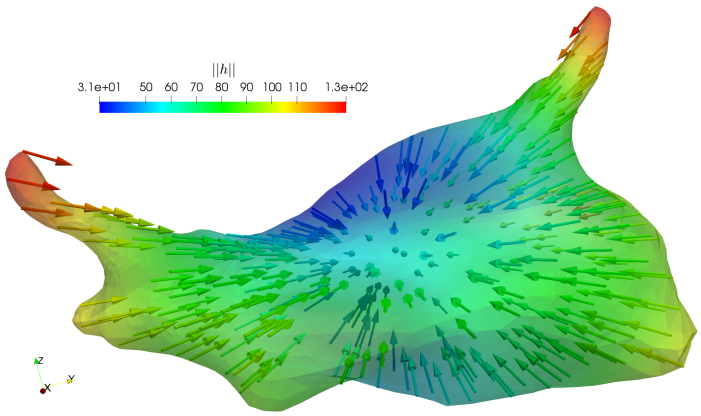

Figure 8: The applied tractions for the microglial cell problem.

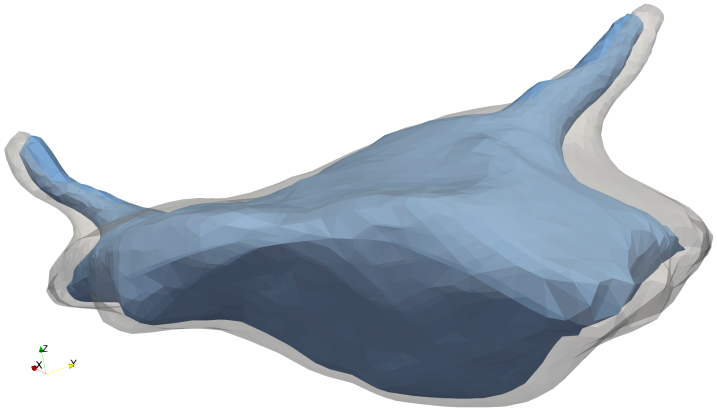

Figure 9: The initial (light grey) and deformed (blue) geometry of the microglial cell before and after tractions are applied.

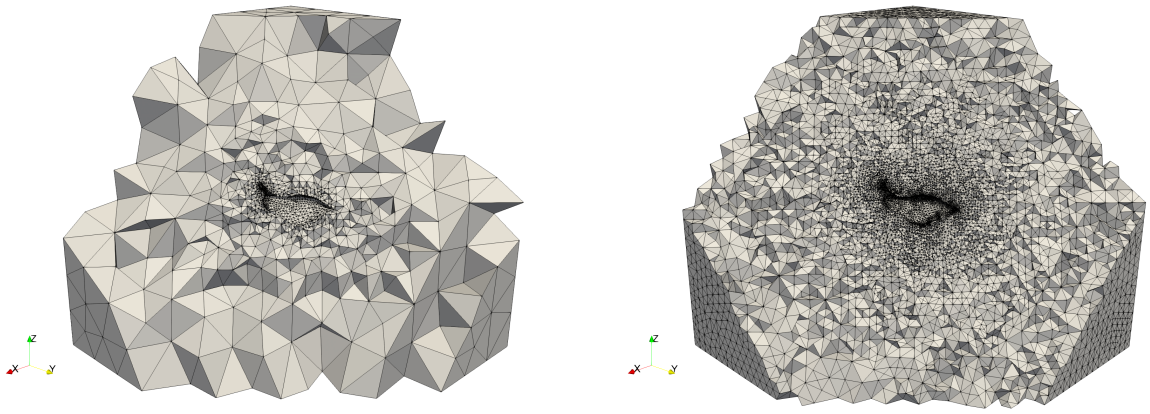

Figure 10: Initial mesh for the microglial cell problem (left) and final adapted mesh after 10 adaptive iterations (right).

initial mesh, the steps

Solve primal PDE → Solve adjoint PDE → Localize error → Adapt mesh

were iteratively performed 10 times. The mesh size field was specified according to equation (35) such that the desired number of elements N in the output mesh is 1.5 times the number of elements in the previous mesh.

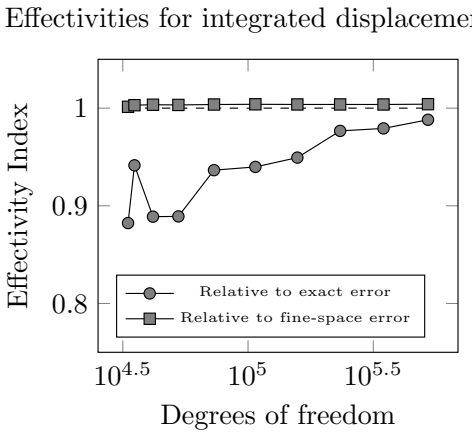

Figure 11: Effectivity indices for the local average displacement QoI $J(\boldsymbol{U})$ for the microglial cell problem.

We again consider the "exact error" $\mathcal{E} = J(\boldsymbol{U}) - J^h(\boldsymbol{U}_H^h)$ and the error $\mathcal{E}_h = J^h(\boldsymbol{U}^h) - J^h(\boldsymbol{U}_H^h)$ with respect to the functional evaluated on the fine mesh, and their effectivity indices $\mathcal{I} = \frac{\eta}{\mathcal{E}}$ and $I_h = \frac{\eta}{\mathcal{E}_h}$, respectively. Here η denotes the error estimate computed by (28). We again expect that the functional will converge at the rate $k = 2$ and use the correction value $\alpha = \frac{3}{4}$.

Figure 11 plots the effectivity index $\mathcal{I}$ relative to the "exact error" and the effectivity index I_h relative to the fine space error. The small distance away from 1 in the discrete effectivity index $\mathcal{I}_h$ is associated with the linearization error introduced by the adjoint problem. Additionally, the ability of the error estimate to recover the "exact error" as $H \to 0$ compared to the reference value is demonstrated by the effectivity $\mathcal{I}$.

Figure 12 displays the evolution of various errors throughout the adaptive process. In particular, the "exact error" $\mathcal{E}$ and the estimated error η are very close, as previously noted by the effectivity index $\mathcal{I}$. As for the Cook's membrane problem the estimated error bound $\hat{\eta}$ overestimates the error, but not to a drastic degree. Finally, we remark that the corrected functional value, computed as $J^*(\boldsymbol{U}_H^h) = J^h(\boldsymbol{U}_H^h) + \eta$, is nearly two orders of magnitude more accurate at the final adaptive step, demonstrating the usefulness of adjoint-based error estimation.

Finally, we plot the evolution of the "exact error" for two adaptive strategies in Figure 13. We compare the convergence of errors for uniform mesh refinement and the developed adjoint-based adaptive scheme. The error is converging at a faster rate for the adjoint-based adaptive scheme. Further, the adjoint-based adaptive scheme achieves the same accuracy as the uniform refinement scheme with nearly an order of magnitude fewer degrees of freedom at around $110,000$ degrees freedom. This demonstrates the utility of adjoint-based adaptivity for solid mechanics problems.

6. Conclusions

In this paper, we have developed an adjoint-based error estimation procedure for nonlinear finite deformation elasticity using a stabilized finite element method, where we have utilized a recently developed PU-based error localization strategy. We have demonstrated the ability of this approach to accurately estimate functional errors for a two-dimensional model problem. Further, we have demonstrated the utility of adaptive adjoint-based analysis in the context of a three-dimensional example problem motivated by the study of biological tissues. Future work includes analytically and numerically investigating the differences

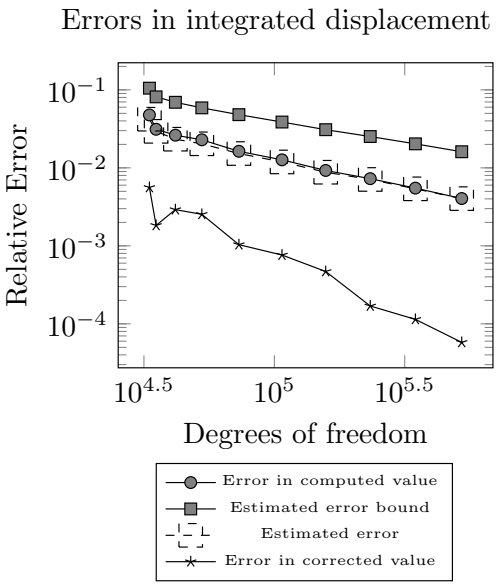

Figure 12: Errors for the local average displacement QoI $J(\boldsymbol{U})$ for the microglial cell problem.

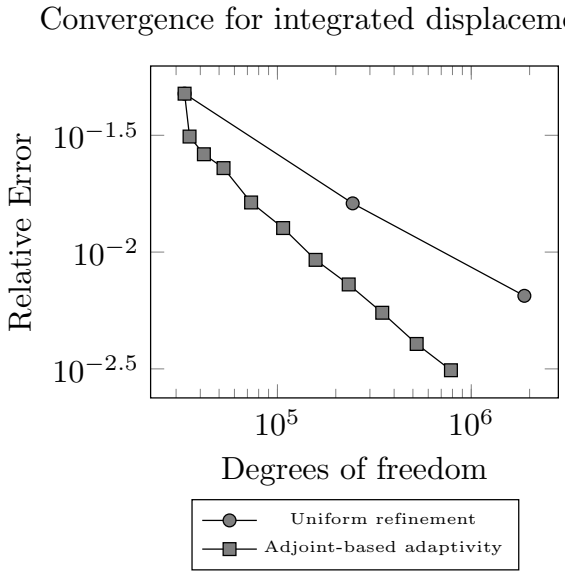

Figure 13: Error convergence using uniform mesh refinement (Uniform) and adjoint-based adaptivity (Goal) for the local average displacement QoI $J(\boldsymbol{U})$ for the microglial cell problem.

in the PU-based localization approach as compared to a more classical strong-form localization approach for localized point-wise quantities of interest.

7. Acknowledgements

The authors acknowledge the support of IBM Corporation in the performance of this research. The computing resources of the Center for Computational Innovations, at Rensselaer Polytechnic Institute, are also acknowledged. The development of tools used in this work was partly supported by the U.S. Department of Energy, Office of Science, Office of Advanced Scientific Computing Research, under award DE-SC00066117 (FASTMath SciDAC Institute). The authors would like to thank Li Dong for providing the discrete geometric model used for the microglial cell example.

[1] Frédéric Alauzet, Xiangrong Li, E Seegyoung Seol, and Mark S Shephard. Parallel anisotropic 3d mesh adaptation by mesh modification. *Engineering with Computers*, 21(3):247–258, 2006.

[2] I Babuška, T Strouboulis, A Mathur, and CS Upadhyay. Pollution-error in the h-version of the finite-element method and the local quality of a-posteriori error estimators. *Finite Elements in Analysis and Design*, 17(4):273–321, 1994.

[3] Wolfgang Bangerth and Rolf Rannacher. *Adaptive finite element methods for differential equations*. Birkhäuser, 2013.

[4] Timothy J. Barth and Mats G. Larson. A posteriori error estimates for higher order godunov finite volume methods on unstructured meshes. Technical report, Complex Applications III, R. Herbin and D. Kroner (Eds), HERMES Science Publishing Ltd, 2002.

[5] Roland Becker and Rolf Rannacher. An optimal control approach to a posteriori error estimation in finite element methods. *Acta numerica*, 10:1–102, 2001.

[6] Ramzy Boussetta, Thierry Coupez, and Lionel Fourment. Adaptive remeshing based on a posteriori error estimation for forging simulation. *Computer methods in applied mechanics and engineering*, 195(48):6626–6645, 2006.

[7] Malte Braack and Alexandre Ern. A posteriori control of modeling errors and discretization errors. *Multiscale Modeling & Simulation*, 1(2):221–238, 2003.

[8] Qiushi Chen, Jakob T Ostien, and Glen Hansen. Automatic differentiation for numerically exact computation of tangent operators in small-and large-deformation computational inelasticity. In *TMS 2014: 143rd Annual Meeting & Exhibition*, pages 289–296. Springer, 2014.

[9] Eric C Cyr, John Shadid, and Tim Wildey. Approaches for adjoint-based a posteriori analysis of stabilized finite element methods. *SIAM Journal on Scientific Computing*, 36(2):A766–A791, 2014.

[10] Dennis E Discher, Paul Janmey, and Yu-li Wang. Tissue cells feel and respond to the stiffness of their substrate. *Science*, 310(5751):1139–1143, 2005.

[11] Li Dong and Assad A Oberai. Recovery of cellular traction in three-dimensional nonlinear hyperelastic matrices. *Computer Methods in Applied Mechanics and Engineering*, 314:296–313, 2017.

[12] Krzysztof J Fidkowski and David L Darmofal. Output-based adaptive meshing using triangular cut cells. Technical report, Aerospace Computational Design Laboratory, Dept. of Aeronautics & Astronautics, Massachusetts Institute of Technology, 2006.

[13] Krzysztof J Fidkowski and David L Darmofal. Review of output-based error estimation and mesh adaptation in computational fluid dynamics. *AIAA journal*, 49(4):673–694, 2011.

[14] S Sh Ghorashi, J Amani, AS Bagherzadeh, and T Rabczuk. Goal-oriented error estimation and mesh adaptivity in three-dimentional elasticity problems. *WCCM XI-ECCM V-ECFD VI, Barcelona, Spain*, 2014.

[15] S Sh Ghorashi and T Rabczuk. Goal-oriented error estimation and mesh adaptivity in 3d elastoplasticity problems. *International Journal of Fracture*, 203(1-2):3–19, 2017.

[16] Michael B Giles and Endre Süli. Adjoint methods for PDEs: a posteriori error analysis and postprocessing by duality. *Acta numerica*, 11:145–236, 2002.

[17] Octavio Andres González-Estrada, E Nadal, JJ Ródenas, Pierre Kerfriden, Stéphane Pierre-Alain Bordas, and FJ Fuenmayor. Mesh adaptivity driven by goal-oriented locally equilibrated superconvergent patch recovery. *Computational Mechanics*, 53(5):957–976, 2014.

[18] Brian N Granzow, Mark S Shephard, and Assad A Oberai. Output-based error estimation and mesh adaptation for variational multiscale methods. *Computer Methods in Applied Mechanics and Engineering*, 322:441–459, 2017.

[19] Ralf Hartmann and Paul Houston. Adaptive discontinuous galerkin finite element methods for the compressible euler equations. *Journal of Computational Physics*, 183(2):508–532, 2002.

[20] Daniel A Ibanez, E Seegyoung Seol, Cameron W Smith, and Mark S Shephard. Pumi: Parallel unstructured mesh infrastructure. *ACM Transactions on Mathematical Software (TOMS)*, 42(3):17, 2016.

[21] Ottmar Klaas, Antoinette Maniatty, and Mark S Shephard. A stabilized mixed finite element method for finite elasticity.: Formulation for linear displacement and pressure interpolation. *Computer Methods in Applied Mechanics and Engineering*, 180(1):65–79, 1999.

[22] Fredrik Larsson, Peter Hansbo, and Kenneth Runesson. Strategies for computing goal-oriented a posteriori error measures in non-linear elasticity. *International Journal for Numerical Methods in Engineering*, 55(8):879–894, 2002.

[23] Wesley R Legant, Jordan S Miller, Brandon L Blakely, Daniel M Cohen, Guy M Genin, and Christopher S Chen. Measurement of mechanical tractions exerted by cells in three-dimensional matrices. *Nature methods*, 7(12):969–971, 2010.

[24] Xiangrong Li, Mark S Shephard, and Mark W Beall. 3d anisotropic mesh adaptation by mesh modification. *Computer methods in applied mechanics and engineering*, 194(48):4915–4950, 2005.

[25] James Lu. *An a posteriori error control framework for adaptive precision optimization using discontinuous Galerkin finite element method*. PhD thesis, Massachusetts Institute of Technology, 2005.

[26] Antoinette M Maniatty, Yong Liu, Ottmar Klaas, and Mark S Shephard. Higher order stabilized finite element method for hyperelastic finite deformation. *Computer methods in applied mechanics and engineering*, 191(13):1491–1503, 2002.
[27] Marian Nemec and Michael J Aftosmis. Adjoint error estimation and adaptive refinement for embedded-boundary cartesian meshes. *AIAA Paper*, 4187:2007, 2007.
[28] JT Ostien, JW Foulk, A Mota, and MG Veilleux. A 10-node composite tetrahedral finite element for solid mechanics. *International Journal for Numerical Methods in Engineering*, 107(13):1145–1170, 2016.
[29] Matthew J Paszek, Nastaran Zahir, Kandice R Johnson, Johnathon N Lakins, Gabriela I Rozenberg, Amit Gefen, Cynthia A Reinhart-King, Susan S Margulies, Micah Dembo, David Boettiger, et al. Tensional homeostasis and the malignant phenotype. *Cancer cell*, 8(3):241–254, 2005.
[30] J Peraire and AT Patera. Bounds for linear-functional outputs of coercive partial differential equations: local indicators and adaptive refinement. *Studies in Applied Mechanics*, 47:199–216, 1998.
[31] Serge Prudhomme and J Tinsley Oden. On goal-oriented error estimation for elliptic problems: application to the control of pointwise errors. *Computer Methods in Applied Mechanics and Engineering*, 176(1-4):313–331, 1999.
[32] E Rabizadeh, A Saboor Bagherzadeh, and T Rabczuk. Adaptive thermo-mechanical finite element formulation based on goal-oriented error estimation. *Computational Materials Science*, 102:27–44, 2015.
[33] Binoj Ramesh and Antoinette M Maniatty. Stabilized finite element formulation for elastic–plastic finite deformations. *Computer Methods in Applied Mechanics and Engineering*, 194(6):775–800, 2005.
[34] Rolf Rannacher and F-T Suttmeier. A feed-back approach to error control in finite element methods: application to linear elasticity. *Computational Mechanics*, 19(5):434–446, 1997.
[35] Rolf Rannacher and F-T Suttmeier. A posteriori error control in finite element methods via duality techniques: Application to perfect plasticity. *Computational mechanics*, 21(2):123–133, 1998.
[36] Rolf Rannacher and Franz-Theo Suttmeier. A posteriori error estimation and mesh adaptation for finite element models in elasto-plasticity. *Computer Methods in Applied Mechanics and Engineering*, 176(1-4):333–361, 1999.
[37] Thomas Richter and Thomas Wick. Variational localizations of the dual weighted residual estimator. *Journal of Computational and Applied Mathematics*, 279:192–208, 2015.
[38] Erwin Stein, Marcus Rüter, and Stephan Ohnimus. Error-controlled adaptive goal-oriented modeling and finite element approximations in elasticity. *Computer methods in applied mechanics and engineering*, 196(37):3598–3613, 2007.
[39] Cedric Taylor and Paul Hood. A numerical solution of the navier-stokes equations using the finite element technique. *Computers & Fluids*, 1(1):73–100, 1973.
[40] David A Venditti and David L Darmofal. Adjoint error estimation and grid adaptation for functional outputs: Application to quasi-one-dimensional flow. *Journal of Computational Physics*, 164(1):204–227, Oct 2000.
[41] David A. Venditti and David L. Darmofal. Grid adaptation for functional outputs: Application to two-dimensional inviscid flows. *Journal of Computational Physics*, 176(1):40–69, Feb 2002.
[42] David A. Venditti and David L. Darmofal. Anisotropic grid adaptation for functional outputs: Application to two-dimensional viscous flows. *J. Comput. Phys.*, 187(1):22–46, May 2003.
[43] JP Whiteley and SJ Tavener. Error estimation and adaptivity for incompressible hyperelasticity. *International Journal for Numerical Methods in Engineering*, 99(5):313–332, 2014.
[44] Thomas Wick. Goal functional evaluations for phase-field fracture using PU-based DWR mesh adaptivity. *Computational Mechanics*, 57(6):1017–1035, 2016.